2008

Quantitative Constraints On The Transport Properties Of Hot Partonic Matter From Semi-Inclusive Single High Transverse Momentum Pion Suppression In Au+Au Collisions At √sNN = 200 GeV

Andrew Marshall Adare

Gyöngyi Baksay

László A. Baksay

Klaus Dehmelt

Marcus Hohlmann

See next page for additional authors

Authors

Andrew Marshall Adare, Gyöngyi Baksay, László A. Baksay, Klaus Dehmelt, Marcus Hohlmann, S. Rembeczki, and PHENIX Collaboration

Quantitative constraints on the transport properties of hot partonic matter from semi-inclusive single high transverse momentum pion suppression in Au+Au collisions at $\sqrt{s_{NN}} = 200$ GeV

A. Adare,[8] S. Afanasiev,[22] C. Aidala,[9] N. N. Ajitanand,[49] Y. Akiba,[43,44] H. Al-Bataineh,[38] J. Alexander,[49] A. Al-Jamel,[38] K. Aoki,[28,43] L. Aphecetche,[51] R. Armendariz,[38] S. H. Aronson,[3] J. Asai,[44] E. T. Atomssa,[29] R. Averbeck,[50] T. C. Awes,[39] B. Azmoun,[3] V. Babintsev,[18] G. Baksay,[14] L. Baksay,[14] A. Baldisseri,[11] K. N. Barish,[4] P. D. Barnes,[31] B. Bassalleck,[37] S. Bathe,[4] S. Batsouli,[9,39] V. Baublis,[42] F. Bauer,[4] A. Bazilevsky,[3] S. Belikov,[3,21,*] R. Bennett,[50] Y. Berdnikov,[46] A. A. Bickley,[8] M. T. Bjorndal,[9] J. G. Boissevain,[31] H. Borel,[11] K. Boyle,[50] M. L. Brooks,[31] D. S. Brown,[38] D. Bucher,[34] H. Buesching,[3] V. Bumazhnov,[18] G. Bunce,[3,44] J. M. Burward-Hoy,[31] S. Butsyk,[31,50] S. Campbell,[50] J.-S. Chai,[23] B. S. Chang,[58] J.-L. Charvet,[11] S. Chernichenko,[18] J. Chiba,[24] C. Y. Chi,[9] M. Chiu,[9,19] I. J. Choi,[58] T. Chujo,[55] P. Chung,[49] A. Churyn,[18] V. Cianciolo,[39] C. R. Cleven,[16] Y. Cobigo,[11] B. A. Cole,[9] M. P. Comets,[40] P. Constantin,[21,31] M. Csanád,[13] T. Csörgő,[25] T. Dahms,[50] K. Das,[15] G. David,[3] M. B. Deaton,[1] K. Dehmelt,[14] H. Delagrange,[51] A. Denisov,[18] D. d'Enterria,[9] A. Deshpande,[44,50] E. J. Desmond,[3] O. Dietzsch,[47] A. Dion,[50] M. Donadelli,[47] J. L. Drachenberg,[1] O. Drapier,[29] A. Drees,[50] A. K. Dubey,[57] A. Durum,[18] V. Dzhordzhadze,[4,52] Y. V. Efremenko,[39] J. Egdemir,[50] F. Ellinghaus,[8] W. S. Emam,[4] A. Enokizono,[17,30] H. En'yo,[43,44] B. Espagnon,[40] S. Esumi,[54] K. O. Eyser,[4] D. E. Fields,[37,44] M. Finger,[5,22] M. Finger, Jr.,[5,22] F. Fleuret,[29] S. L. Fokin,[27] B. Forestier,[32] Z. Fraenkel,[57,*] J. E. Frantz,[9,50] A. Franz,[3] A. D. Frawley,[15] K. Fujiwara,[43] Y. Fukao,[28,43] S.-Y. Fung,[4] T. Fusayasu,[36] S. Gadrat,[32] I. Garishvili,[52] F. Gastineau,[51] M. Germain,[51] A. Glenn,[8,52] H. Gong,[50] M. Gonin,[29] J. Gosset,[11] Y. Goto,[43,44] R. Greiner de Cassagnac,[29] N. Grau,[21] S. V. Greene,[55] M. Groose Perdekamp,[19,44] T. Gunji,[7] H.-Å. Gustafsson,[33] T. Hachiya,[17,43] A. Hadj Henni,[51] C. Haegemann,[37] J. S. Haggerty,[3] M. N. Hagiwara,[1] H. Hamagaki,[7] R. Han,[41] H. Harada,[17] E. P. Hartouni,[30] K. Haruna,[17] M. Harvey,[3] E. Haslum,[33] K. Hasuko,[43] R. Hayano,[7] M. Heffner,[30] T. K. Hemmick,[50] T. Hester,[4] J. M. Heuser,[43] X. He,[16] H. Hiejima,[19] J. C. Hill,[21] R. Hobbs,[37] M. Hohlmann,[14] M. Holmes,[55] W. Holzmann,[49] K. Homma,[17] B. Hong,[26] T. Horaguchi,[43,53] D. Hornback,[52] M. G. Hur,[23] T. Ichihara,[43,44] K. Imai,[28,43] J. Imrek,[12] M. Inaba,[54] Y. Inoue,[43,45] D. Isenhower,[1] L. Isenhower,[1] M. Ishihara,[43] T. Isobe,[7] M. Issah,[49] A. Isupov,[22] B. V. Jacak,[50,†] J. Jia,[9] J. Jin,[9] O. Jinnouchi,[44] B. M. Johnson,[3] K. S. Joo,[35] D. Jouan,[40] F. Kajihara,[7,43] S. Kametani,[7,56] N. Kamihara,[43,53] J. Kamin,[50] M. Kaneta,[44] J. H. Kang,[58] H. Kanou,[43,53] T. Kawagishi,[54] D. Kawall,[44] A. V. Kazantsev,[27] S. Kelly,[8] A. Khanzadeev,[42] J. Kikuchi,[56] D. H. Kim,[35] D. J. Kim,[58] E. Kim,[48] Y.-S. Kim,[23] E. Kinney,[8] A. Kiss,[13] E. Kistenev,[3] A. Kiyomichi,[43] J. Klay,[30] C. Klein-Boesing,[34] L. Kochenda,[42] V. Kochetkov,[18] B. Komkov,[42] M. Konno,[54] D. Kotchetkov,[4] A. Kozlov,[57] A. Král,[10] A. Kravitz,[9] P. J. Kroon,[3] J. Kubart,[5,20] G. J. Kunde,[31] N. Kurihara,[7] K. Kurita,[45,43] M. J. Kweon,[26] Y. Kwon,[52,58] G. S. Kyle,[38] R. Lacey,[49] Y.-S. Lai,[9] J. G. Lajoie,[21] A. Lebedev,[21] Y. Le Bornec,[40] S. Leckey,[50] D. M. Lee,[31] M. K. Lee,[58] T. Lee,[48] M. J. Leitch,[31] M. A. L. Leite,[47] B. Lenzi,[47] H. Lim,[48] T. Liška,[10] A. Litvinenko,[22] M. X. Liu,[31] X. Li,[6] X. H. Li,[4] B. Love,[55] D. Lynch,[3] C. F. Maguire,[55] Y. I. Makdisi,[3] A. Malakhov,[22] M. D. Malik,[37] V. I. Manko,[27] Y. Mao,[41,43] L. Mašek,[5,20] H. Masui,[54] F. Matathias,[9,50] M. C. McCain,[19] M. McCumber,[50] P. L. McGaughey,[31] Y. Miake,[54] P. Mikeš,[5,20] K. Miki,[54] T. E. Miller,[55] A. Milov,[50] S. Mioduszewski,[3] G. C. Mishra,[16] M. Mishra,[2] J. T. Mitchell,[3] M. Mitrovski,[49] A. Morreale,[4] D. P. Morrison,[3] J. M. Moss,[31] T. V. Moukhanova,[27] D. Mukhopadhyay,[55] J. Murata,[43,45] S. Nagamiya,[24] Y. Nagata,[54] J. L. Nagle,[8] M. Naglis,[57] I. Nakagawa,[43,44] Y. Nakamiya,[17] T. Nakamura,[17] K. Nakano,[43,53] J. Newby,[30] M. Nguyen,[50] B. E. Norman,[31] A. S. Nyanin,[27] J. Nystrand,[33] E. O'Brien,[3] S. X. Oda,[7] C. A. Ogilvie,[21] H. Ohnishi,[43] I. D. Ojha,[55] H. Okada,[28,43] K. Okada,[44] M. Oka,[54] O. O. Omiwade,[1] A. Oskarsson,[33] I. Otterlund,[33] M. Ouchida,[17] K. Ozawa,[7] R. Pak,[3] D. Pal,[55] A. P. T. Palounek,[31] V. Pantuev,[50] V. Papavassiliou,[38] J. Park,[48] W. J. Park,[26] S. F. Pate,[38] H. Pei,[21] J.-C. Peng,[19] H. Pereira,[11] V. Peresedov,[22] D. Yu. Peressounko,[27] C. Pinkenburg,[3] R. P. Pisani,[3] M. L. Purschke,[3] A. K. Purwar,[31,50] H. Qu,[16] J. Rak,[21,37] A. Rakotozafindrabe,[29] I. Ravinovich,[57] K. F. Read,[39,52] S. Rembeczki,[14] M. Reuter,[50] K. Reygers,[34] V. Riabov,[42] Y. Riabov,[42] G. Roche,[32] A. Romana,[29,*] M. Rosati,[21] S. S. E. Rosendahl,[33] P. Rosnet,[32] P. Rukoyatkin,[22] V. L. Rykov,[43] S. S. Ryu,[58] B. Sahlmueller,[34] N. Saito,[28,43,44] T. Sakaguchi,[3,7,56] S. Sakai,[54] H. Sakata,[17] V. Samsonov,[42] H. D. Sato,[28,43] S. Sato,[3,24,54] S. Sawada,[24] J. Seele,[8] R. Seidl,[19] V. Semenov,[18] R. Seto,[4] D. Sharma,[57] T. K. Shea,[3] I. Shein,[18] A. Shevel,[42,49] T.-A. Shibata,[43,53] K. Shigaki,[17] M. Shimomura,[54] T. Shohjoh,[54] K. Shoji,[28,43] A. Sickles,[50] C. L. Silva,[47] D. Silvermyr,[39] C. Silvestre,[11] K. S. Sim,[26] C. P. Singh,[2] V. Singh,[2] S. Skutnik,[21] M. Slunečka,[5,22] W. C. Smith,[1] A. Soldatov,[18] R. A. Soltz,[30] W. E. Sondheim,[31] S. P. Sorensen,[52] I. V. Sourikova,[3] F. Staley,[11] P. W. Stankus,[39] E. Stenlund,[33] M. Stepanov,[38] A. Ster,[25] S. P. Stoll,[3] T. Sugitate,[17] C. Suire,[40] J. P. Sullivan,[31] J. Sziklai,[25] T. Tabaru,[44] S. Takagi,[54] E. M. Takagui,[47] A. Taketani,[43,44] K. H. Tanaka,[24] Y. Tanaka,[36] K. Tanida,[43,44] M. J. Tannenbaum,[3] A. Taranenko,[49] P. Tarján,[12] T. L. Thomas,[37] M. Togawa,[28,43] A. Toia,[50] J. Tojo,[43] L. Tomášek,[20] H. Torii,[43] R. S. Towell,[1] V.-N. Tram,[29] I. Tserruya,[57] Y. Tsuchimoto,[17,43] S. K. Tuli,[2] H. Tydesjö,[33] N. Tyurin,[18] C. Vale,[21] H. Valle,[55] H. W. van Hecke,[31] J. Velkovska,[55] R. Vertesi,[12] A. A. Vinogradov,[27] M. Virius,[10] V. Vrba,[20] E. Vznuzdaev,[42] M. Wagner,[28,43] D. Walker,[50] X. R. Wang,[38] Y. Watanabe,[43,44] J. Wessels,[34] S. N. White,[3] N. Willis,[40] D. Winter,[9] C. L. Woody,[3] M. Wysocki,[8] W. Xie,[4,44] Y. L. Yamaguchi,[56] A. Yanovich,[18] Z. Yasin,[4] J. Ying,[16] S. Yokkaichi,[43,44] G. R. Young,[39] I. Younus,[37] I. E. Yushmanov,[27] W. A. Zajc,[9] O. Zaudtke,[34] C. Zhang,[9,39] S. Zhou,[6] J. Zimányi,[25,*] and L. Zolin[22]

(PHENIX Collaboration)

[1]*Abilene Christian University, Abilene, Texas 79699, USA*

[2]*Department of Physics, Banaras Hindu University, Varanasi 221005, India*

[3]*Brookhaven National Laboratory, Upton, New York 11973-5000, USA*

[4]*University of California-Riverside, Riverside, California 92521, USA*
[5]*Charles University, Ovocný trh 5, Praha 1, 116 36, Prague, Czech Republic*
[6]*China Institute of Atomic Energy (CIAE), Beijing, People's Republic of China*
[7]*Center for Nuclear Study, Graduate School of Science, University of Tokyo, 7-3-1 Hongo, Bunkyo, Tokyo 113-0033, Japan*
[8]*University of Colorado, Boulder, Colorado 80309, USA*
[9]*Columbia University, New York, New York 10027 and Nevis Laboratories, Irvington, New York 10533, USA*
[10]*Czech Technical University, Zikova 4, 166 36 Prague 6, Czech Republic*
[11]*Dapnia, CEA Saclay, F-91191, Gif-sur-Yvette, France*
[12]*Debrecen University, H-4010 Debrecen, Egyetem tér 1, Hungary*
[13]*ELTE, Eötvös Loránd University, H-1117 Budapest, Pázmány P. s. 1/A, Hungary*
[14]*Florida Institute of Technology, Melbourne, Florida 32901, USA*
[15]*Florida State University, Tallahassee, Florida 32306, USA*
[16]*Georgia State University, Atlanta, Georgia 30303, USA*
[17]*Hiroshima University, Kagamiyama, Higashi-Hiroshima 739-8526, Japan*
[18]*IHEP Protvino, State Research Center of Russian Federation, Institute for High Energy Physics, Protvino, RU-142281, Russia*
[19]*University of Illinois at Urbana-Champaign, Urbana, Illinois 61801, USA*
[20]*Institute of Physics, Academy of Sciences of the Czech Republic, Na Slovance 2, 182 21 Prague 8, Czech Republic*
[21]*Iowa State University, Ames, Iowa 50011, USA*
[22]*Joint Institute for Nuclear Research, RU-141980 Dubna, Moscow Region, Russia*
[23]*KAERI, Cyclotron Application Laboratory, Seoul, Korea*
[24]*KEK, High Energy Accelerator Research Organization, Tsukuba, Ibaraki 305-0801, Japan*
[25]*KFKI Research Institute for Particle and Nuclear Physics of the Hungarian Academy of Sciences (MTA KFKI RMKI), H-1525 Budapest 114, P. O. Box 49, Budapest, Hungary*
[26]*Korea University, Seoul, 136-701, Korea*
[27]*Russian Research Center "Kurchatov Institute," Moscow, Russia*
[28]*Kyoto University, Kyoto 606-8502, Japan*
[29]*Laboratoire Leprince-Ringuet, Ecole Polytechnique, CNRS-IN2P3, Route de Saclay, F-91128, Palaiseau, France*
[30]*Lawrence Livermore National Laboratory, Livermore, California 94550, USA*
[31]*Los Alamos National Laboratory, Los Alamos, New Mexico 87545, USA*
[32]*LPC, Université Blaise Pascal, CNRS-IN2P3, Clermont-Fd, F-63177 Aubiere Cedex, France*
[33]*Department of Physics, Lund University, Box 118, SE-221 00 Lund, Sweden*
[34]*Institut für Kernphysik, University of Muenster, D-48149 Muenster, Germany*
[35]*Myongji University, Yongin, Kyonggido 449-728, Korea*
[36]*Nagasaki Institute of Applied Science, Nagasaki-shi, Nagasaki 851-0193, Japan*
[37]*University of New Mexico, Albuquerque, New Mexico 87131, USA*
[38]*New Mexico State University, Las Cruces, New Mexico 88003, USA*
[39]*Oak Ridge National Laboratory, Oak Ridge, Tennessee 37831, USA*
[40]*IPN-Orsay, Universite Paris Sud, CNRS-IN2P3, BP1, F-91406, Orsay, France*
[41]*Peking University, Beijing, People's Republic of China*
[42]*PNPI, Petersburg Nuclear Physics Institute, Gatchina, Leningrad region, RU-188300, Russia*
[43]*RIKEN, The Institute of Physical and Chemical Research, Wako, Saitama 351-0198, Japan*
[44]*RIKEN BNL Research Center, Brookhaven National Laboratory, Upton, New York 11973-5000, USA*
[45]*Physics Department, Rikkyo University, 3-34-1 Nishi-Ikebukuro, Toshima, Tokyo 171-8501, Japan*
[46]*Saint Petersburg State Polytechnic University, St. Petersburg, Russia*
[47]*Universidade de São Paulo, Instituto de Física, Caixa Postal 66318, São Paulo CEP05315-970, Brazil*
[48]*System Electronics Laboratory, Seoul National University, Seoul, Korea*
[49]*Chemistry Department, Stony Brook University, Stony Brook, SUNY, New York 11794-3400, USA*
[50]*Department of Physics and Astronomy, Stony Brook University, SUNY, Stony Brook, New York 11794, USA*
[51]*SUBATECH (Ecole des Mines de Nantes, CNRS-IN2P3, Université de Nantes) BP 20722-44307, Nantes, France*
[52]*University of Tennessee, Knoxville, Tennessee 37996, USA*
[53]*Department of Physics, Tokyo Institute of Technology, Oh-okayama, Meguro, Tokyo 152-8551, Japan*
[54]*Institute of Physics, University of Tsukuba, Tsukuba, Ibaraki 305, Japan*
[55]*Vanderbilt University, Nashville, Tennessee 37235, USA*
[56]*Waseda University, Advanced Research Institute for Science and Engineering, 17 Kikui-cho, Shinjuku-ku, Tokyo 162-0044, Japan*
[57]*Weizmann Institute, Rehovot 76100, Israel*
[58]*Yonsei University, IPAP, Seoul 120-749, Korea*
(Received 10 January 2008; published 24 June 2008)

The PHENIX experiment has measured the suppression of semi-inclusive single high-transverse-momentum π^0's in Au+Au collisions at $\sqrt{s_{NN}} = 200$ GeV. The present understanding of this suppression is in terms of energy loss of the parent (fragmenting) parton in a dense color-charge medium. We have performed a quantitative comparison between various parton energy-loss models and our experimental data. The statistical point-to-point uncorrelated as well as correlated systematic uncertainties are taken into account in the comparison. We detail this methodology and the resulting constraint on the model parameters, such as the initial color-charge density dN^g/dy, the medium transport coefficient $\langle\hat{q}\rangle$, or the initial energy-loss parameter ϵ_0. We find that high-transverse-momentum π^0 suppression in Au+Au collisions has sufficient precision to constrain these model-dependent parameters at the ±20–25% (one standard deviation) level. These constraints include only the experimental uncertainties, and further studies are needed to compute the corresponding theoretical uncertainties.

DOI: 10.1103/PhysRevC.77.064907 PACS number(s): 25.75.Dw

I. INTRODUCTION

Heavy-ion collisions at very high energy are of interest due to the formation of a novel partonic medium approximately the size of a large nucleus, but with an energy density exceeding that of normal nuclei by considerably more than an order of magnitude. At such high energy densities, it is believed that quarks and gluons are no longer confined in hadrons but may be constituents of a quark-gluon plasma with characteristics of a near-perfect fluid (for a detailed review see Ref. [1]). Experiments at the Relativistic Heavy Ion Collider (RHIC) have already demonstrated that a very hot and dense, strongly interacting medium is created in Au+Au collisions at $\sqrt{s_{NN}} =$ 200 GeV [2]. The goal is now to quantitatively determine the properties of this medium.

Important properties of the medium include the density of color charges as well as the exchange of transverse momentum between parton probes and the medium. In rare events, in addition to the creation of the medium, there can also be a hard scattering (high-Q^2 process) between the colliding partons that, at leading order, sends two high-energy quark or gluon partons in opposite transverse directions. These high-energy partons can be utilized to probe both the color-charge density of the medium and the coupling strength between the parton and the medium. There are various calculational frameworks for modeling these interactions (for a detailed review see Ref. [3]).

In this article, we consider four specific calculations of parton energy loss (discussed below): the parton quenching model (PQM) [4], the Gyulassy-Levai-Vitev (GLV) model [5], the Wicks-Horowitz-Djordjevic-Gyulassy (WHDG) model [6], and the Zhang-Owens-Wang-Wang (ZOWW) model [7]. We detail a quantitative method of assessing the sensitivity of the latest measurements to the input parameters of these models that characterize the initial parton density or medium transport coefficients.

II. EXPERIMENTAL RESULTS

During the 2004 data-taking period at the Relativistic Heavy Ion Collider, the PHENIX experiment recorded an integrated luminosity of 0.24 nb^{-1} in $\sqrt{s_{NN}} = 200$ GeV Au+Au collisions, which extends the measurement of π^0 to much higher p_T than previous data sets allowed. The results and further details of this measurement are given in Ref. [9]. A brief description is given below.

The PHENIX experiment measures π^0's via the two-photon decay mode with two types of highly segmented ($\Delta\eta \times \Delta\phi \approx 0.01 \times 0.01$) electromagnetic calorimeters (EMCal) located at the radial distance of approximately 5 m from the vertex [8]. One is a lead scintillator sampling calorimeter (PbSc), which covers the geometrical acceptance of $|\eta| < 0.35$ and $\Delta\phi = 3/4\pi$. The other is a lead glass Cerenkov calorimeter (PbGl), whose geometrical coverage is $|\eta| < 0.35$ and $\Delta\phi = \pi/4$. The energy resolution of the PbSc and PbGl calorimeters as determined from test beam measurements are given by $8.1\%/\sqrt{E(\text{GeV})} \oplus 2.1\%$ and $5.9\%/\sqrt{E(\text{GeV})} \oplus 0.8\%$, respectively. The energy calibration of the EMCal modules is based on the measured position of the π^0 mass peak, the deposited energy of minimum ionizing particles that traverse the calorimeter, and the ratio of energy to momentum that is expected to be about 1 for electrons identified by the ring-imaging Cerenkov detector. The systematic uncertainty on the energy scale is ∼1%, which corresponds to ∼7–12% uncertainty on the invariant π^0 yield over the p_T range of the measurement.

Neutral pions were reconstructed in their $\pi^0 \to \gamma\gamma$ decay channel. Photon candidates are identified by applying particle identification cuts based mainly on the shower shape. The invariant mass for all photon-pair combinations within one event that satisfy cuts on the energy asymmetry $|E_{\gamma 1} - E_{\gamma 2}|/|E_{\gamma 1} + E_{\gamma 2}| < 0.8$ were calculated in bins of p_T. The combinatorial background is determined by combining into pairs uncorrelated photons from different events with similar centrality, reaction plane, and vertex location.

The raw π^0 yield was obtained by integrating the mass peak region of the invariant mass distribution after subtracting the combinatorial background. The raw spectra are corrected for the detector response (energy resolution), the reconstruction efficiency, and occupancy effects (e.g., overlapping clusters). These corrections are made by embedding simulated single π^0's from a full GEANT simulation of the PHENIX detector into real events and analyzing the embedded π^0 events with the same analysis cuts as used with real events.

After computing the invariant yields in Au+Au collisions [9], the medium effects are quantified using the nuclear modification factor (R_{AA}). R_{AA} is the ratio between the

*Deceased
†PHENIX Spokesperson: jacak@skipper.physics.sunysb.edu

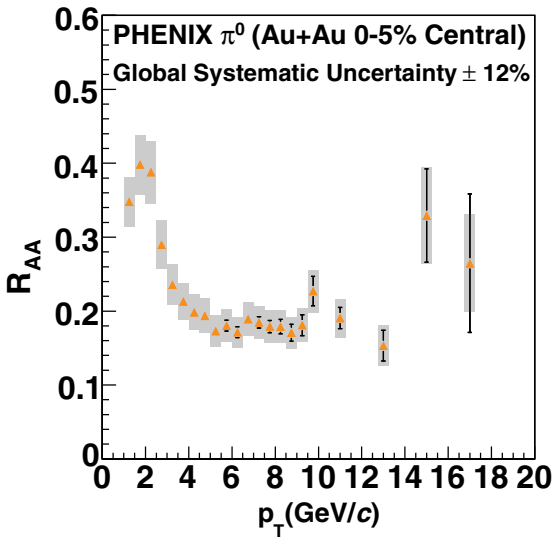

FIG. 1. (Color online) The π^0 nuclear suppression factor $R_{\rm AA}$ as a function of transverse momentum for 0–5% Au+Au collisions at $\sqrt{s_{NN}} = 200$ GeV. Point-to-point uncorrelated statistical and systematic uncertainties are shown as uncertainty bars. Correlated systematic uncertainties are shown as gray boxes around the data points. The global scale factor systematic uncertainty is ±12%.

measured yield and the expected yield for pointlike processes scaled from the $p+p$ result and is defined as:

$$\mathrm{R_{AA}}(p_T) = \frac{\left(1/N_{\rm AA}^{\rm evt}\right) d^2 N_{\rm AA}^{\pi^0}/dp_T dy}{\langle T_{\rm AA}\rangle d^2\sigma_N^{\pi^0}/dp_T dy}, \qquad (1)$$

where $\langle T_{\rm AA}\rangle$ is the average Glauber nuclear overlap function for the Au+Au centrality bin under consideration

$$\langle T_{\rm AA}\rangle \equiv \frac{\int T_{\rm AA}(\mathbf{b}) d\mathbf{b}}{\int \left(1 - e^{-\sigma_{NN}^{\rm inel} T_{\rm AA}(\mathbf{b})}\right) d\mathbf{b}} = \left\langle N_{\rm coll}^{\sigma_{NN}}\right\rangle / \sigma_{NN}^{\rm inel}, \qquad (2)$$

where $\langle N_{\rm coll}^{\sigma_{NN}}\rangle$ is the average number of inelastic nucleon-nucleon collisions for the Au+Au centrality bin under consideration calculated with inelastic nucleon-nucleon cross section $\sigma_{NN}^{\rm inel}$.

The measured nuclear modification factors for 0–5% central Au+Au reactions at $\sqrt{s_{NN}} = 200$ GeV are shown in Fig. 1 and tabulated in Table I with statistical and systematic uncertainties. The systematic uncertainties fall into three categories. We denote type A uncertainties as systematic uncertainties that are uncorrelated from point to point. Type A systematic uncertainties are added in quadrature with statistical uncertainties and are shown as uncertainty bars. Partially correlated point-to-point systematic uncertainties are broken into a 100% correlated component, referred to as type B, and the above mentioned type A. The type B uncertainties are shown as gray boxes. The sources of type B uncertainties are discussed in detail in Ref. [9] and are dominated by energy scale uncertainties but also have contributions from photon shower merging at the highest p_T (≈15–20 GeV/c). There are also global systematic uncertainties, referred to as type C uncertainties, that are globally correlated systematic uncertainties (i.e., where all data points move by the same multiplicative factor). The type C uncertainties are ±12% and derive from uncertainties in the calculated nuclear thickness function and from the $p+p$ absolute normalization.

TABLE I. The π^0 nuclear suppression factor $R_{\rm AA}$ as a function of transverse momentum for 0-5% Au+Au collisions at $\sqrt{s_{NN}} =$ 200 GeV. The type A, B, and C uncertainties are tabulated for each point.

p_T (GeV/c)	$R_{\rm AA}$	Type A uncertainty	Type B uncertainty	Type C uncertainty
1.25	0.347	±0.007	±0.033	±0.041
1.75	0.398	±0.007	±0.040	±0.047
2.25	0.387	±0.007	±0.042	±0.046
2.75	0.289	±0.006	±0.032	±0.034
3.25	0.235	±0.005	±0.027	±0.028
3.75	0.21	±0.005	±0.024	±0.025
4.25	0.198	±0.005	±0.024	±0.023
4.75	0.193	±0.006	±0.023	±0.023
5.25	0.172	±0.006	±0.021	±0.020
5.75	0.180	±0.007	±0.021	±0.021
6.25	0.171	±0.007	±0.020	±0.020
6.75	0.189	±0.007	±0.022	±0.022
7.25	0.184	±0.008	±0.022	±0.022
7.75	0.179	±0.008	±0.021	±0.021
8.25	0.178	±0.010	±0.021	±0.021
8.75	0.170	±0.011	±0.020	±0.020
9.25	0.180	±0.014	±0.022	±0.021
9.75	0.226	±0.019	±0.028	±0.027
11.00	0.190	±0.014	±0.026	±0.022
13.00	0.153	±0.020	±0.027	±0.018
15.00	0.329	±0.063	±0.065	±0.039
17.00	0.264	±0.093	±0.065	±0.031

III. THEORETICAL CALCULATIONS

The parton quenching model (PQM) [4] encodes the dissipative properties of the system in terms of a single transport coefficient, often referred to as $\hat{q}$, obtained as the product of the parton-medium cross section times the color-charge density. The average $\hat{q}$ quantifies the average squared transverse momentum transferred from the medium to the parton per mean free path. The PQM model is a Monte Carlo program constructed using the quenching weights from BDMPS [10,11]. BDMPS is a perturbative calculation explicitly including only coherent radiative energy loss for the parton via gluon bremsstrahlung. The PQM model incorporates a realistic transverse collision geometry, though with a static medium. It is also notable that the PQM model does not include initial state multiple scattering or modified nuclear parton distribution functions (PDF's).

The Gyulassy-Levai-Vitev (GLV) [5] model is a formalism developed to calculate in-medium gluon bremsstrahlung. An analytic expression is derived for the single gluon emission spectrum to all orders in opacity, assuming an infrared cutoff given by the plasmon frequency. Thus, within this framework, one can extract the local color-charge density. The color-charge density is written simply as dN^g/dy, assuming a completely

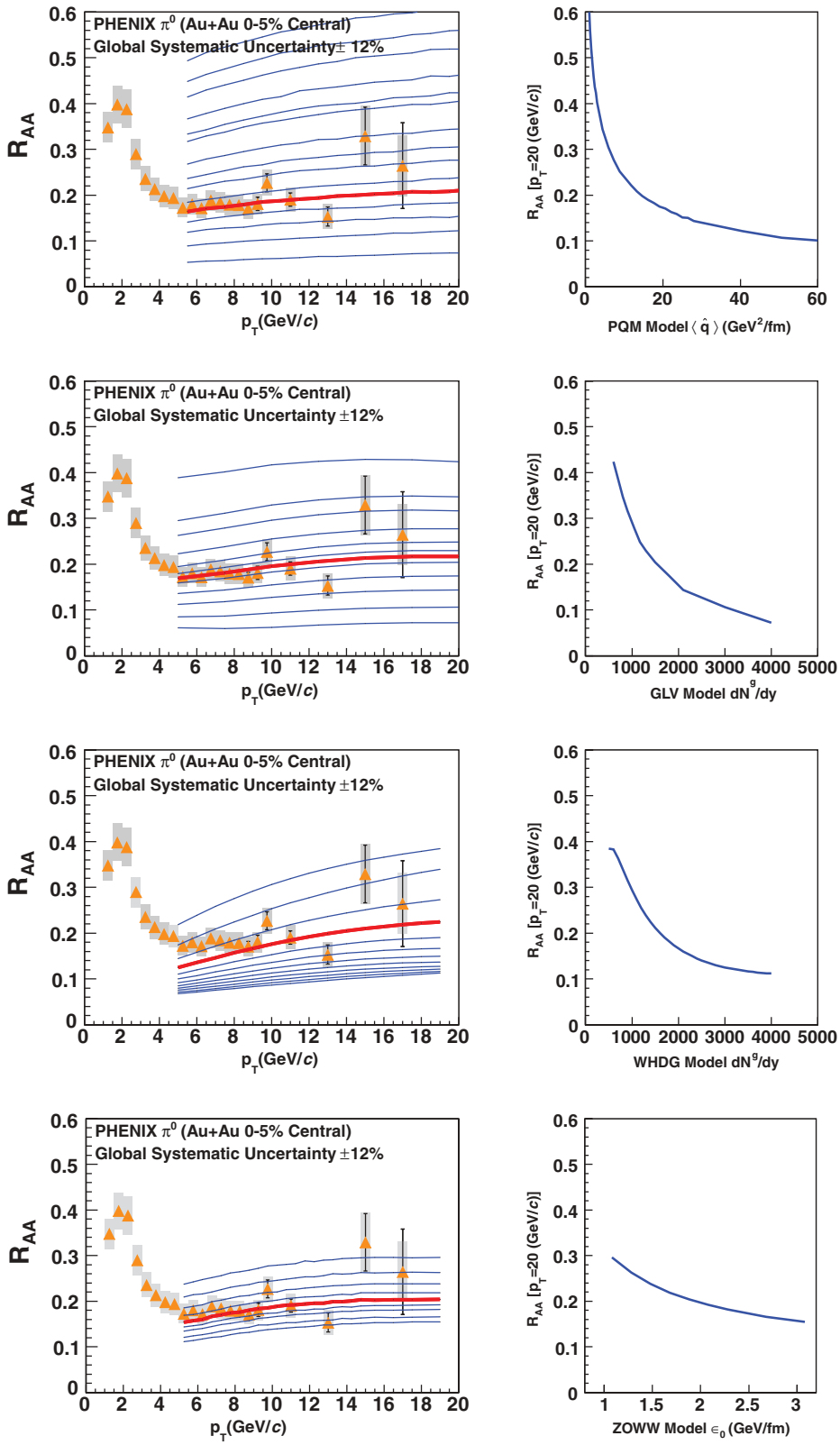

FIG. 2. (Color online) Left panels show π^0 $R_{\rm AA}$ for 0–5% Au+Au collisions at $\sqrt{s_{NN}} = 200$ GeV and predictions from PQM [4], GLV [12], WHDG [6], and ZOWW [7] models with (from top to bottom) $\langle \hat{q} \rangle$ values of 0.3, 0.9, 1.2, 1.5, 2.1, 2.9, 4.4, 5.9, 7.4, 10.3, 13.2, 17.7, 25.0, 40.5, 101.4 GeV^2/fm; dN^g/dy values of 600, 800, 900, 1050, 1175, 1300, 1400, 1500, 1800, 2100, 3000, 4000; dN^g/dy values of 500, 800, 1100, 1400, 1700, 2000, 2300, 2600, 2900, 3200, 3500, 3800; and ϵ_0 values of 1.08, 1.28, 1.48, 1.68, 1.88, 2.08, 2.28, 2.68, 3.08 GeV/fm. Red lines indicate the best fit cases of (top) $\langle \hat{q} \rangle = 13.2$, (upper middle) $dN^g/dy = 1400$, (lower middle) $dN^g/dy = 1400$, and (bottom) $\epsilon_0 = 1.88$ GeV/fm. Right panels show $R_{\rm AA}$ at $p_{\rm T} = 20$ GeV/c.

gluonic medium, or an equivalent $dN^{q,g}/dy$ for a mixture of quarks and gluons. In Ref. [12], using a realistic transverse collision geometry, the authors calculate *a priori*, without energy loss, the single fixed geometrical average path length from the production point to the medium edge, $\langle L \rangle_{\rm prod}$, and use it to calculate the parton energy loss in a Bjorken expanding medium [13]. The calculation also incorporates initial-state multiple scattering effects and modified nuclear PDF's.

The Wicks-Horowitz-Djordjevic-Gyulassy (WHDG) [6] model utilizes the generalized GLV formalism [15] for

radiative energy loss described above. In addition, their calculation includes a convolution of radiative energy loss and collisional energy-loss mechanisms. A realistic transverse collision geometry with a Bjorken time expansion is utilized, and then a full distribution of parton paths through the medium is calculated. The WHDG model does not yet include initial-state multiple scattering or modified PDF's.

The Zhang-Owens-Wang-Wang (ZOWW) [7] calculations incorporate a next-to-leading-order perturbative QCD parton model with modified jet fragmentation functions. The calculation explicitly includes only radiative energy loss. A hard-sphere transverse collision geometry with a one-dimensional expanding medium is utilized. The calculation also incorporates initial-state multiple scattering effects and modified nuclear PDF's.

The top left panel of Fig. 2 shows a comparison of the experimental data with calculated results from the PQM energy-loss model (as described in Ref. [4]) corresponding to different $\langle\hat{q}\rangle$ values [16]. Note that only a subset of all the calculations corresponding to different $\langle\hat{q}\rangle$ values are shown in the figure for clarity. The upper right panel shows the π^0 suppression factor predicted at $p_T = 20$ GeV/c from the PQM model as a function of the $\langle\hat{q}\rangle$ value. One can see that as the $\langle\hat{q}\rangle$ increases, the additional suppression becomes smaller (i.e., saturates). This saturation effect was noted in Ref. [14], and interpreted as a result of the dominance of preferential surface emission.

The other panels of Fig. 2 show similar comparisons of the experimental data with calculated results utilizing the GLV numerical calculation framework (as described in Ref. [12]) corresponding to different dN^g/dy values [17]; the WHDG calculational framework (as described in Ref. [6]) corresponding to different dN^g/dy values [18]; and the ZOWW calculational framework (as detailed in Ref. [7]) corresponding to different ϵ_0 values [19]. Note that all calculations are shown only for $p_T > 5$ GeV/c as that is where the calculations are considered applicable.

In Fig. 3, the same π^0 suppression factor predicted at $p_T = 20$ GeV/c from the PQM model as a function of the $\langle\hat{q}\rangle$ value is shown, but in this case with a log-x and log-y scale. The $R_{\rm AA} \approx 0.75/\sqrt{\langle\hat{q}\rangle}$ with $\langle\hat{q}\rangle$ in units of GeV^2/fm over the range $5 < \langle\hat{q}\rangle < 100$. This means that over this range for a given fractional change in $\langle\hat{q}\rangle$ there is always the same fractional change in $R_{\rm AA}$ (i.e., $\Delta\langle\hat{q}\rangle/\langle\hat{q}\rangle \approx 2.0 \times \Delta R_{\rm AA}/R_{\rm AA}$).

IV. COMBINED RESULTS

The task is now to detail how the experimental uncertainties (statistical and systematic) constrain the model parameters that are reflected in the suppression factors. As described previously, the uncertainties of the measured points are separated into type A (p_T-uncorrelated, statistical $\oplus$ systematic, σ_i), type B (p_T-correlated, σ_{b_i}, boxes on Fig. 1), type C (normalization, uniform fractional shift for all points, σ_c), where the σ's represent the standard deviations of the assumed Gaussian distributed uncertainties. With the predicted theory value $\mu_i(p)$ for each data point calculated for different values of the input parameter p, we perform a least-squares fit the to the theory

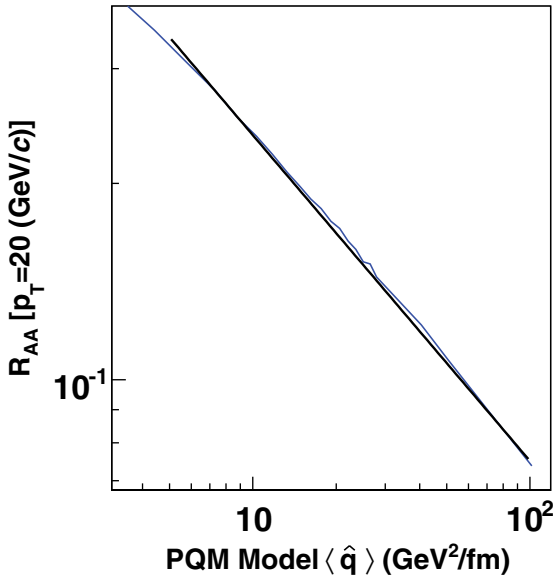

FIG. 3. (Color online) The nuclear suppression factors at $p_T = 20$ GeV/c for PQM as a function of $\langle\hat{q}\rangle$ are shown as a blue line with a log-x and log-y display. Also shown is the functional form $\Delta\langle\hat{q}\rangle/\langle\hat{q}\rangle \approx 2.0 \times \Delta R_{\rm AA}/R_{\rm AA}$) over the range $5 < \langle\hat{q}\rangle < 100$ GeV^2/fm.

by finding the values of $p, \epsilon_b, \epsilon_c$, that minimize:

$$\tilde{\chi}^2(\epsilon_b, \epsilon_c, p) = \left\{ \sum_{i=1}^{n} \frac{[y_i + \epsilon_b \sigma_{b_i} + \epsilon_c y_i \sigma_c - \mu_i(p)]^2}{\tilde{\sigma}_i^2} + \epsilon_b^2 + \epsilon_c^2 \right\}, \quad (3)$$

where ϵ_b and ϵ_c are the fractions of the type B and C systematic uncertainties that all points are displaced together and where $\tilde{\sigma}_i = \sigma_i(y_i + \epsilon_b \sigma_{b_i} + \epsilon_c y_i \sigma_c)/y_i$ is the point-to-point random uncertainty scaled by the multiplicative shift in y_i such that the fractional uncertainty is unchanged under systematic shifts, which is true for the present measurement. For clarity of presentation, the derivation of Eq. (3) (above) is given in Appendix A.

For any fixed values of ϵ_b, ϵ_c, Eq. (3) follows the χ^2 distribution with $n+2$ degrees of freedom, for testing the theoretical predictions $\mu_i(p)$, because it is the sum of $n+2$ Gaussian distributed random variables. The best fit, $\tilde{\chi}^2_{\rm min}$, the minimum of $\tilde{\chi}^2(\epsilon_b, \epsilon_c, p)$ by variation of ϵ_b, ϵ_c, and p, is found by standard methods (for example, using a MINUIT type minimization algorithm) and should follow the χ^2 distribution with $n-1$ degrees of freedom. The correlated uncertainties of the best fit parameters are estimated in the Gaussian approximation by $\tilde{\chi}^2(\epsilon_b, \epsilon_c, p) = \tilde{\chi}^2_{\rm min} + N^2$ for N standard deviation (σ) uncertainties.

The present experimental type B uncertainties have point-to-point correlations whose exact correlation matrix is difficult to evaluate precisely. Thus, we consider two limiting correlation cases. The first is where the type B uncertainties are 100% correlated, i.e., all points move in the same direction by the same fraction of their respective type B uncertainty. The second is where the type B uncertainties are correlated such that the

low p_T and high p_T points may shift with opposite sign (and linearly scaled in between), thus tilting the R_{AA} either upward or downward as a function of p_T. The minimum $\tilde{\chi}^2$ of the two cases is used for each constraint.

We take as a first example the resulting theory predictions from the PQM model. For each calculation characterized by the $\langle\hat{q}\rangle$, we calculate $\tilde{\chi}^2$. We determine this value by varying ϵ_b and ϵ_c (the systematic offsets) until we obtain the minimum $\tilde{\chi}^2$. These values are shown in Fig. 4 in the top panel. One can see that the overall lowest $\tilde{\chi}^2$ value corresponds to $\langle\hat{q}\rangle \approx 13\ \mathrm{GeV}^2/\mathrm{fm}$.

We then calculate the p value for the $\tilde{\chi}^2$ [the minimum of Eq. (3)], where the p value is defined as:

$$p\ \text{value} = \int_{\tilde{\chi}^2}^{\infty} \chi^2_{(n_d)}(z)dz, \tag{4}$$

where $\chi^2_{(n_d)}$ is the chi-square distribution with the appropriate number of degrees of freedom, n_d [20]. This calculation is valid because the goodness-of-fit statistic $\tilde{\chi}^2$ follows a standard χ^2 distribution. Note that p value is the probability, under the assumption that the hypothesis is correct, of randomly obtaining data with a worse fit to the hypothesis than the experimental data under test [20]. These p value s are shown in the middle panel of Fig. 4.

We find the overall minimum (or best) $\tilde{\chi}^2$ and then compute which $\langle\hat{q}\rangle$ scenarios are 1 and 2 standard deviations away from this minimum. The PQM transport coefficient $\langle\hat{q}\rangle$ is constrained by the experimental data as $13.2^{+2.1}_{-3.2}$ and $^{+6.3}_{-5.2}$ GeV^2/fm at the 1 and 2 standard deviation levels, respectively. The two standard deviation constraints correspond to the 95% confidence intervals. We note that this range of large $\langle\hat{q}\rangle$ values is currently under intense theoretical debate (see, for example, Ref. [21]). Thus, the quoted $\langle\hat{q}\rangle$ constraint is for the model-dependent parameter of the specific PQM implementation, and relating this parameter to the fundamental value of the mean transverse momentum squared exchange per unit length traversed may substantially lower the value.

We apply the identical procedure to the GLV, WHDG, and ZOWW calculations and show those results in Figs. 5, 6, and 7. For the GLV calculations this results in a constraint of $dN^g/dy = 1400^{+270}_{-150}$ and $^{+510}_{-290}$ at the 1 and 2 standard deviation levels, respectively. All of these constraint results are summarized in Table II. Constraints for the WHDG model are $dN^g/dy = 1400^{+200}_{-375}$ and $^{+600}_{-540}$ at the 1 and 2 standard deviation levels, respectively. Constraints for the ZOWW model are $\epsilon_0 = 1.9^{+0.2}_{-0.5}$ and $^{+0.7}_{-0.6}$ at the 1 and 2 standard deviation levels, respectively.

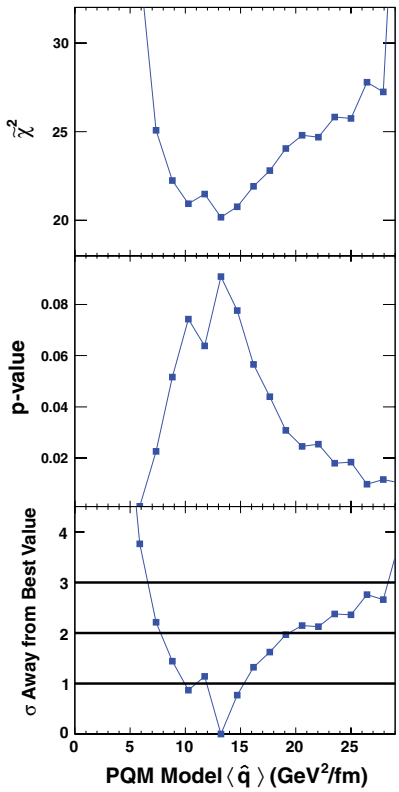

FIG. 4. (Color online) The statistical analysis results from the comparison of the PQM model with the π^0 $R_{AA}(p_T)$ experimental data. The top panel shows the modified $\tilde{\chi}^2$ for different values of the PQM $\langle\hat{q}\rangle$. The middle panel shows the computed p value directly from the modified $\tilde{\chi}^2$ as shown above. The bottom panel shows the number of standard deviations (σ) away from the minimum (best) $\langle\hat{q}\rangle$ parameter value for the PQM model calculations.

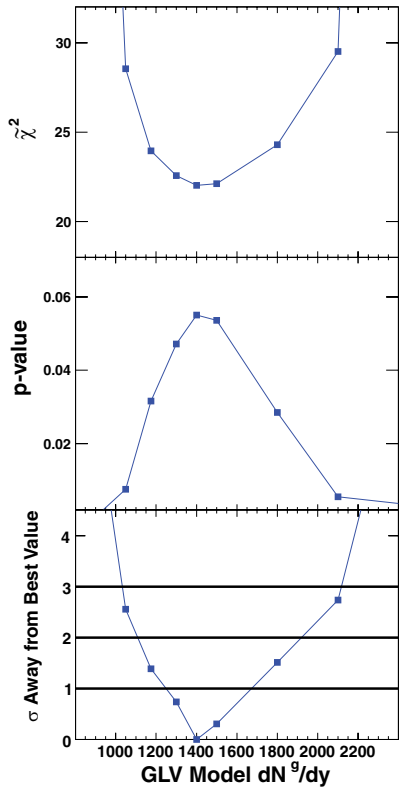

FIG. 5. (Color online) The statistical analysis results from the comparison of the GLV model with the $\pi^0 R_{AA}(p_T)$ experimental data. The top panel shows the modified $\tilde{\chi}^2$ for different values of the GLV dN^g/dy. The middle panel shows the computed p value directly from the modified $\tilde{\chi}^2$ as shown above. The bottom panel shows the number of standard deviations (σ) away from the minimum (best) dN^g/dy parameter value for the GLV model calculations.

TABLE II. Quantitative constraints on the model parameters from the PQM, GLV, WHDG, and ZOWW models and a linear functional form fit.

Model name	Model parameter	1 standard deviation uncertainty	2 standard deviation uncertainty	Maximum p value (%)
PQM	$\langle\hat{q}\rangle = 13.2$ GeV^2/fm	$+2.1 - 3.2$	$+6.3 - 5.2$	9.0
GLV	$dN^g/dy = 1400$	$+270 - 150$	$+510 - 290$	5.5
WHDG	$dN^g/dy = 1400$	$+200 - 375$	$+600 - 540$	1.3
ZOWW	$\epsilon_0 = 1.9$ GeV/fm	$+0.2 - 0.5$	$+0.7 - 0.6$	7.8
Linear	b (intercept) $= 0.168$	$+0.033 - 0.032$	$+0.065 - 0.066$	11.6
	m (slope) $= 0.0017$ (c/GeV)	$+0.0035 - 0.0039$	$+0.0070 - 0.0076$	

For each of the above fits, there is a best fit value of ϵ_b and ϵ_c corresponding to the parameters in Eq. (3). For completeness, these values are for PQM, GLV, WHDG, and ZOWW, $\epsilon_b = 0.6$ and $\epsilon_c = -0.3$, $\epsilon_b = 0.7$ and $\epsilon_c = -0.0$, $\epsilon_b = 2.1$ and $\epsilon_c = -1.5$, and $\epsilon_b = 1.1$ and $\epsilon_c = -0.6$, respectively. All of the models considered here have a steeper p_T dependence of R_{AA} than the experimental data. Thus, the best fit is obtained within the type B uncertainties by tilting the $R_{\rm AA}$.

It is notable that although there is a well-defined overall minimum in the modified $\tilde{\chi}^2$ for all four models, the maximum p value in each case is different. In the PQM, GLV, and ZOWW models the maximum p value s are approximately 9.0%, 5.5%, and 7.8%, respectively. However, in the WHDG model the maximum p value is substantially smaller at 1.3%. This is due to the fact that the WHDG model has a steeper p_T dependence of the nuclear modification factor $R_{\rm AA}$ (regardless of parameter input) than the other models and also steeper than the experimental data points.

The identical best value of dN^g/dy for the GLV and WHDG calculations is interesting, because the inclusion of important collisional energy loss in WHDG leads to the naive expectation that a smaller color-charge density would

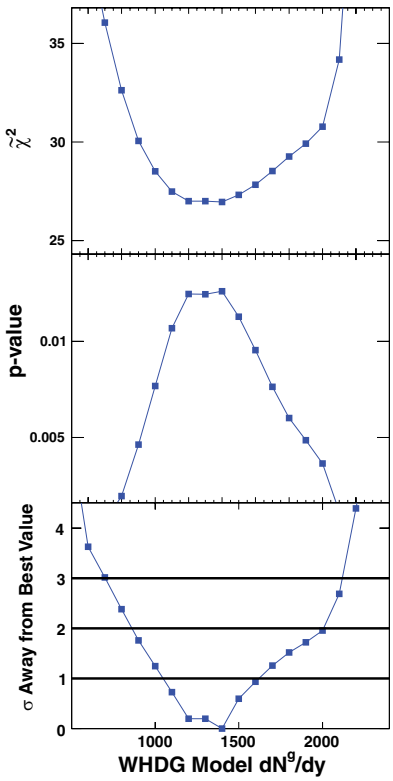

FIG. 6. (Color online) The statistical analysis results from the comparison of the WHDG model with the $\pi^0 R_{\rm AA}(p_T)$ experimental data. The top panel shows the modified $\tilde{\chi}^2$ for different values of the WHDG dN^g/dy. The middle panel shows the computed p value directly from the modified $\tilde{\chi}^2$ as shown above. The bottom panel shows the number of standard deviations (σ) away from the minimum (best) dN^g/dy parameter value for the WHDG model calculations.

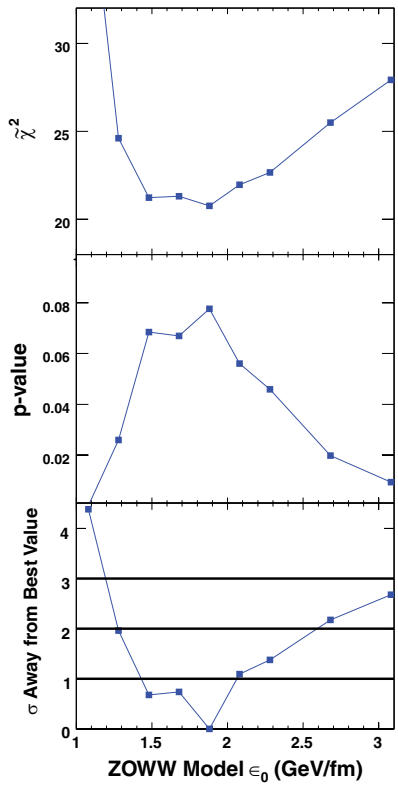

FIG. 7. (Color online) The statistical analysis results from the comparison of the ZOWW model with the $\pi^0 R_{\rm AA}(p_T)$ experimental data. The top panel shows the modified $\tilde{\chi}^2$ for different values of the ZOWW ϵ_0. The middle panel shows the computed p value directly from the modified $\tilde{\chi}^2$ as shown above. The bottom panel shows the number of standard deviations (σ) away from the minimum (best) ϵ_0 parameter value for the ZOWW model calculations.

be needed for a similar suppression. However, the different treatments of the distribution of paths through the medium may be compensating for this effect. Further theoretical studies are needed to disentangle the physics implications of the shape differences and the similar best dN^g/dy from GLV and WHDG. For all the models considered, the relevant parameter constraint is approximately a ±20–25% uncertainty at the 1 standard deviation level.

It is also interesting to inquire what simple linear fit function best describes the experimental data for $p_T >$ 5 GeV/c. The identical procedure to that described above is applied to the function $R_{AA}(p_T) = \mathrm{b} + \mathrm{m} \times p_T$ to determine the best values for the two parameters. The best fit line and the envelope of lines with 1 standard deviation uncertainties are shown in Fig. 8. The results including all types of uncertainties are $b(\text{intercept}) = 0.168^{+0.033}_{-0.032}$ and $\mathrm{m(slope)} = 0.0017^{+0.0035}_{-0.0039}$ (GeV/c). The uncertainties on these parameters are correlated as shown by the 1, 2, and 3 standard deviation contours in Fig. 9.

Thus the data are consistent with a completely flat p_T dependence of R_{AA} for $p_T >$5 GeV/c (i.e., $m = 0$) within 1 standard deviation uncertainties. The maximum p value for this simple linear function fit is 11.6%.

The p value s for all models considered are less than 12%. It is notable that the five highest p_T points ($p_T > 9.5$ GeV/c) contribute over 70% to the total $\tilde{\chi}^2$. As a check on the influence of these points on the extracted parameter values, we have repeated the above procedure to the restricted range $5 < p_T < 9.5$ GeV/c. We find the following new constraints: PQM model

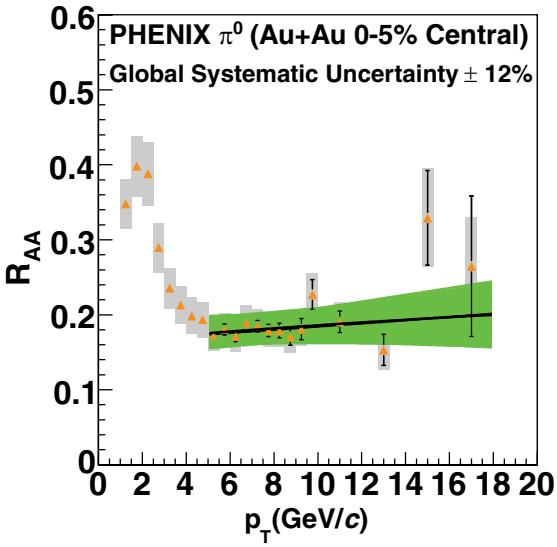

FIG. 8. (Color online) The π^0 nuclear suppression factor R_{AA} as a function of transverse momentum for 0–5% Au+Au collisions at $\sqrt{s_{NN}} = 200$ GeV. Point-to-point uncorrelated statistical and systematic uncertainties are shown as uncertainty bars. Correlated systematic uncertainties are shown as gray boxes around the data points. The global scale factor systematic uncertainty is quoted as text. Also shown are the best fit and the envelope of lines with one standard deviation uncertainty for a simple linear fit function constrained by the statistical and systematic uncertainties.

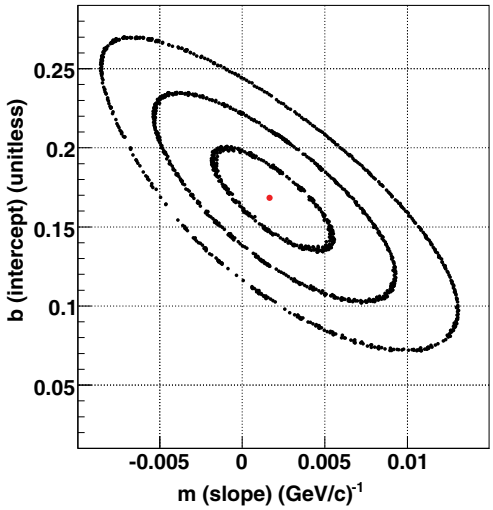

FIG. 9. (Color online) Shown are the best fit values for m(slope) and b(intercept) as constrained by the experimental data. Also shown are the 1, 2, and 3 standard deviation uncertainty contours.

$\langle\hat{q}\rangle = 13.2^{+1.8}_{-4.2}$ GeV^2/fm; GLV model $dN^g/dy = 1400^{+200}_{-210}$; WHDG model $dN^g/dy = 1000^{+300}_{-170}$; ZOWW model $\epsilon_0 = 1.5^{+0.5}_{-0.2}$ GeV/fm; simple linear fit $b(\text{intercept}) = 0.170^{+0.034}_{-0.034}$ and $\mathrm{m(slope)} = 0.0013^{+0.0047}_{-0.0051}$ (GeV/c). We find that the resulting new constraints are within the 1 standard deviation uncertainties of those quoted for the full p_T range. However, with the restricted range, the p value s increase to 55, 36, 17, 62, and 75% for the PQM model, GLV model, WHDG model, ZOWW model, and the simple linear fit, respectively. Improvements in the data for $p_T > 9.5$ GeV/c expected from future measurements will be crucial in determining whether any of the models discussed provide a statistically valid description of the data over the full range $5 \leqslant p_T \leqslant 20$ GeV/c.

V. SUMMARY AND CONCLUSIONS

In this article, we compared model predictions of parton energy loss with experimental data of semi-inclusive single high-transverse-momentum π^0 suppression in central Au+Au reactions at $\sqrt{s_{NN}} = 200$ GeV. In the comparison, statistical and systematic uncertainties were taken into account. We obtained experimental constraints on model parameters of the color-charge density of the medium or its transport coefficient. These values indicate a large medium density. It is crucial to note that the quoted constraints on these parameters do not include any systematic uncertainties in the models but rather give the limits assuming a "perfect theory" with one unknown parameter, for example, the color-charge density, constrained by the measurements, including the experimental statistical and systematic uncertainties. Additional theoretical systematic uncertainties from the time evolution, energy-loss approximations, and calculation details need further investigation.

ACKNOWLEDGMENTS

We thank the staff of the Collider-Accelerator and Physics Departments at Brookhaven National Laboratory and the staff

of the other PHENIX participating institutions for their vital contributions. We thank W. Horowitz, C. Loizides, I. Vitev, and X.-N. Wang for the theoretical calculation input and useful discussions. We acknowledge support from the Office of Nuclear Physics in the Office of Science of the Department of Energy, the National Science Foundation, Abilene Christian University Research Council, Research Foundation of SUNY, and Dean of the College of Arts and Sciences, Vanderbilt University (USA), Ministry of Education, Culture, Sports, Science, and Technology and the Japan Society for the Promotion of Science (Japan), Conselho Nacional de Desenvolvimento Científico e Tecnológico and Fundação de Amparo à Pesquisa do Estado de São Paulo (Brazil), Natural Science Foundation of China (People's Republic of China), Ministry of Education, Youth and Sports (Czech Republic), Centre National de la Recherche Scientifique, Commissariat à l'Énergie Atomique, and Institut National de Physique Nucléaire et de Physique des Particules (France), Ministry of Industry, Science and Tekhnologies, Bundesministerium für Bildung und Forschung, Deutscher Akademischer Austausch Dienst, and Alexander von Humboldt Stiftung (Germany), Hungarian National Science Fund, OTKA (Hungary), Department of Atomic Energy (India), Israel Science Foundation (Israel), Korea Research Foundation and Korea Science and Engineering Foundation (Korea), Ministry of Education and Science, Russian Academy of Sciences, Federal Agency of Atomic Energy (Russia), VR and the Wallenberg Foundation (Sweden), the U.S. Civilian Research and Development Foundation for the Independent States of the Former Soviet Union, the U.S.-Hungarian NSF-OTKA-MTA, and the U.S.-Israel Binational Science Foundation.

APPENDIX: CONSTRAINT FORMALISM

In the case of only point-to-point uncorrelated uncertainties (statistical and/or systematic), if one assumes they are Gaussian distributed and characterized by σ, the root-mean-square (rms), calculating the best-parameter fit is straightforward via a log-likelihood or least-squares χ^2 method [20].

The likelihood function $\mathcal{L}$ is defined as the *a priori* probability of a given outcome. Let $y_1, y_2, \ldots y_n$ be n samples from a population with normalized probability density function $f(y, \vec{p})$, where $\vec{p}$ represents a vector of k parameters. For instance, y_i could represent a measurement of a cross section at transverse momentum $(p_T)_i$, where the probability density of the measurement is Gaussian distributed about the expectation value $\mu = \langle y \rangle$:

$$f(y, \vec{p}) = \frac{1}{\sqrt{2\pi\sigma^2}} \exp - \left[\frac{(y-\mu)^2}{2\sigma^2} \right]. \tag{A1}$$

If the samples are independent, then the likelihood function is:

$$\mathcal{L} = \prod_i f(y_i, \vec{p}) = \frac{1}{\sigma_1 \sigma_2 \ldots \sigma_n} \frac{1}{\sqrt{2\pi}^n} \exp - \left\{ \sum_{i=1}^{n} \frac{[y_i - \mu_i(\vec{p})]^2}{2\sigma_i^2} \right\}. \tag{A2}$$

However, if the samples are correlated, for example, via correlated systematic uncertainties, then the full covariance matrix must be used

$$V_{ij} = \langle [y_i - \mu_i(\vec{p})][y_j - \mu_j(\vec{p})] \rangle. \tag{A3}$$

Then the likelihood function takes the more general form:

$$\mathcal{L} = \frac{1}{\sqrt{|V|}} \frac{1}{\sqrt{2\pi}^n} \exp - \left\{ \sum_{i=1}^{n} \sum_{j=1}^{n} \frac{[y_i - \mu_i(\vec{p})] V_{ij}^{-1} [y_j - \mu_j(\vec{p})]}{2} \right\}, \tag{A4}$$

where $|V|$ is the determinant of the covariance matrix V. Note that Eq. (A4) reduces to Eq. (A2) if the correlations vanish so that the covariances are zero and V_{ij} is diagonal

$$\begin{aligned} V_{ij} &= \langle [y_i - \mu_i(\vec{p})][y_j - \mu_j(\vec{p})] \rangle \\ &= \delta_{ij} \langle [y_i - \mu_i(\vec{p})]^2 \rangle = \delta_{ij} \sigma_i^2. \end{aligned} \tag{A5}$$

Because Gaussian probability distributions are inevitable (as a consequence of the central limit theorem) and because there is also an important theorem regarding likelihood ratios for composite hypotheses, it is convenient to use the logarithm of the likelihood

$$\begin{aligned} -2 \ln \mathcal{L} = {} & \ln |V| + n \log 2\pi \\ & + \sum_{i=1}^{n} \sum_{j=1}^{n} [y_i - \mu_i(\vec{p})] V_{ij}^{-1} [y_j - \mu_j(\vec{p})]. \end{aligned} \tag{A6}$$

We separate the uncertainties into four classes: type A (point-to-point uncorrelated systematic uncertainties); type B (correlated systematic uncertainties, for which the point-to-point correlation is 100% by construction, because the uncorrelated part has been separated out and included in uncertainty A); type C [overall systematic uncertainties by

which all the points move by the same fraction (i.e., normalization uncertainties)]; and type D (statistical). Categories A and D are simply added in quadrature and represent the total point-to-point uncorrelated uncertainties, denoted σ_i below.

We model a correlated systematic uncertainty as if there were an underlying uncertainty, e.g., absolute momentum scale, which may cause correlated systematic variations Δy_i of the set of measurements, y_i, around their nominal value, that can be represented as a random variable, z_b. The correlated type B variation of the measurements is represented by the displacement of all points from their nominal values by the correlated amounts

$$\Delta y^b(\text{sys})_i \equiv b_i \Delta z_b \tag{A7}$$

$$\langle \Delta y^b(\text{sys})_i \Delta y^b(\text{sys})_j \rangle = b_i b_j \sigma_b^2 \equiv \sigma_{b_i} \sigma_{b_j}, \tag{A8}$$

where $\Delta z_b \equiv z_b - \langle z_b \rangle = z_b$.

Because $\langle z_b \rangle \equiv 0$, $\langle (\Delta z_b)^2 \rangle = \langle z_b^2 \rangle - \langle z_b \rangle^2 = \sigma_b^2$ and the random variable z_b is the same for all i measurements, whereas b_i is a constant of proportionality that may be different for each i. We define $\sigma_{b_i} \equiv b_i \sigma_b$, where $\pm|\sigma_{b_i}|$ is the systematic uncertainty bar shown on each point (gray box on each data point in Fig. 1) and where b_i may be of either sign, as it is possible that one point could move up while its neighbor moves down. The random variable z_b is assumed to have a Gaussian probability distribution $f(z_b)$, with rms σ_b

$$f(z_b) = \frac{1}{\sigma_b \sqrt{2\pi}} \exp - \left[\frac{(\Delta z_b)^2}{2\sigma_b^2} \right]. \tag{A9}$$

The type C variation is independent of the type B variation. It is similarly assumed to be caused by an underlying random variable z_c that results in a systematic displacement of the measurement by an amount Δy_i^c with

$$\Delta y^c(\text{sys})_i / y_i \equiv \Delta z_c \tag{A10}$$

$$\langle (\Delta y^c(\text{sys})_i / y_i)(\Delta y^c(\text{sys})_j / y_j) \rangle = \sigma_c^2, \tag{A11}$$

where by definition σ_c is the same for all points.

We then assume that the likelihood function factorizes as the product of independent Gaussian probabilities as in Eq. (A2) but that the distributions are correlated through their dependence on the random variables z_b and z_c:

$$\mathcal{L} = \prod_i f(y_i; z_b, z_c, \vec{p}) f(z_b) f(z_c) = \frac{1}{\sigma_1 \sigma_2 \ldots \sigma_n \sigma_b \sigma_c} \frac{1}{\sqrt{2\pi}^{(n+2)}} \exp - \left\{ \sum_{i=1}^{n} \frac{[y_i + b_i \Delta z_b + y_i \Delta z_c - \mu_i(\vec{p})]^2}{2\sigma_i^2} + \frac{(\Delta z_b)^2}{2\sigma_b^2} + \frac{(\Delta z_c)^2}{2\sigma_c^2} \right\}. \tag{A12}$$

To account for the type B systematic uncertainty, we allow any given sample of measurements, y_i, corresponding to theoretical predictions $\mu_i(\vec{p})$ to have a correlated variation from their nominal values by an amount corresponding to a certain fraction ϵ_b of the underlying root-mean-square variation of z_b, i.e., $\Delta z_b = \epsilon_b \sigma_b$, such that each point moves by an amount $\Delta y_i^b = b_i \epsilon_b \sigma_b \equiv \epsilon_b \sigma_{b_i}$, the same fraction ϵ_b of its systematic uncertainty bar, and similarly for the type C uncertainty. Then the likelihood function for any outcome, including the variation of ϵ_b and ϵ_c, would be:

$$\mathcal{L} = \frac{1}{\sigma_1 \sigma_2 \ldots \sigma_n \sigma_b \sigma_c} \frac{1}{\sqrt{2\pi}^{(n+2)}} \exp - \left\{ \sum_{i=1}^{n} \frac{[y_i + \epsilon_b \sigma_{b_i} + \epsilon_c y_i \sigma_c - \mu_i(\vec{p})]^2}{2\sigma_i^2} + \frac{\epsilon_b^2}{2} + \frac{\epsilon_c^2}{2} \right\}, \tag{A13}$$

where the last two terms represent $(\Delta z_b)^2/(2\sigma_b^2) = \epsilon_b^2 \sigma_b^2/(2\sigma_b^2)$ and $(\Delta z_c)^2/(2\sigma_c^2) = \epsilon_c^2 \sigma_c^2/(2\sigma_c^2)$ because we assumed the probability of the systematic displacements $f(z_{b,c})$ to be Gaussian. Other probability distributions for the correlated systematic uncertainty could be used. For instance, if $\pm|\sigma_{b_i}|$ had represented full extent systematic uncertainties, with equal probability for any Δz_b, then the $\epsilon_b^2/2$ term and associated normalization constant $1/\sigma_b\sqrt{2\pi}$ would be absent from Eq. (A13).

Then we use the likelihood ratio test to establish the validity or the confidence interval of the theoretical predictions $\mu_i(\vec{p})$. One can use the modified log likelihood

$$-2 \ln \mathcal{L} = \left\{ \sum_{i=1}^{n} \frac{[y_i + \epsilon_b \sigma_{b_i} + \epsilon_c y_i \sigma_c - \mu_i(\vec{p})]^2}{\sigma_i^2} + \epsilon_b^2 + \epsilon_c^2 \right\} \equiv \chi^2(\epsilon_b, \epsilon_c, \vec{p}) \tag{A14}$$

because we will eventually take the ratio of the likelihood of a given set of parameters $\vec{p}$ to the maximum likelihood when all the parameters ϵ_b, ϵ_c, and $\vec{p}$ are varied [the minimum value of Eq. (A15)] so that the terms preceding the exponential in Eq. (A13) cancel because they are not varied. Equation (A15)

follows the χ^2 distribution with $n+2$ degrees of freedom because it is the sum of $n+2$ independent Gaussian distributed random variables [i.e., in statistical terminology $\chi^2(\epsilon_b, \epsilon_c, \vec{p})$ is $\chi^2_{(n+2)}$]. This establishes Eq. (A15) as the χ^2-distributed quantity that we use for least-squares fit to the theoretical predictions, including the systematic uncertainties. Note that Eq. (A15) agrees with Eq. (8) in Ref. [24] in the discussion of fits with correlated systematics. The specific procedure is described in the next paragraph.

First "fit the theory" to the data by minimizing Eq. (A15) by varying all the parameters to find $\hat{\epsilon}_b, \hat{\epsilon}_c, \hat{\vec{p}}$, the values of the parameters that give the overall minimum $\chi^2_{\rm min}$. If the $\chi^2_{\rm min}$ for this fit is acceptable for the $n+2-(m+2) = n-m$ degrees of freedom, where m are the number of parameters in $\vec{p}$, then the theory is not rejected at this level. A confidence interval is then found for testing any other set of k parameters constrained to specific values, $\vec{p}_0$, by again finding the minimum of Eq. (A15) for the k fixed values of $\vec{p}_0$, by letting all the other parameters, including ϵ_b and ϵ_c, vary. For constant values of σ_i, and large values of n, the "likelihood ratio" $-2\ln[\mathcal{L}(\vec{p}_0)/\mathcal{L}(\hat{\vec{p}})] = -2[\ln\mathcal{L}(\vec{p}_0) - \ln\mathcal{L}(\hat{\vec{p}})]$, i.e., $\chi^2(\vec{p}_0) - \chi^2_{\rm min}$ is χ^2 distributed with k degrees of freedom, from which the confidence interval on the parameters can be evaluated. However, in general, the uncertainty on the parameters is estimated in the Gaussian approximation by $\chi^2(\vec{p}_0) = \chi^2_{\rm min} + N^2$ for N standard deviation uncertainties (for example, using a MINUIT-type fitting algorithm [23]).

For the present data, the statistical and random systematic uncertainties are such that the shift in the measurement y_i due to the correlated systematic uncertainties preserves the fractional uncertainty. In this case the maximum likelihood and least-squares methods no longer coincide and we use a least-squares fit of Eq. (A16) instead of Eq. (A15) to estimate the best fit parameters:

$$\tilde{\chi}^2 = \left\{ \sum_{i=1}^{n} \frac{[y_i + \epsilon_b \sigma_{b_i} + \epsilon_c y_i \sigma_c - \mu_i(\vec{p})]^2}{\tilde{\sigma}_i^2} + \epsilon_b^2 + \epsilon_c^2 \right\}, \tag{A15}$$

where $\tilde{\sigma}_i$ is the uncertainty scaled by the multiplicative shift in y_i such that the fractional uncertainty is unchanged under shifts

$$\tilde{\sigma}_i = \sigma_i \left(\frac{y_i + \epsilon_b \sigma_{b_i} + \epsilon_c y_i \sigma_c}{y_i} \right). \tag{A16}$$

[1] B. Muller and J. L. Nagle, Annu. Rev. Nucl. Part. Sci. **56**, 93 (2006).
[2] I. Arsene *et al.*, Nucl. Phys. **A757**, 1 (2005); K. Adcox *et al.*, *ibid.* **184**; B. B. Back *et al.*, *ibid.* **28**; J. Adams *et al.*, *ibid.* **102**.
[3] M. Gyulassy, I. Vitev, X. N. Wang, and B. W. Zhang, *Quark Gluon Plasma 3*, edited by R. C. Hwa and X. N. Wang (World Scientific, Singapore, 2004).
[4] A. Dainese, C. Loizides, and G. Paic, Eur. Phys. J. C **38**, 461 (2005); C. Loizides, *ibid.* **49**, 339 (2007).
[5] M. Gyulassy, P. Levai, and I. Vitev, Nucl. Phys. **B571**, 197 (2000).
[6] W. A. Horowitz, S. Wicks, M. Djordjevic, and M. Gyulassy, in preparation; S. Wicks, W. Horowitz, M. Djordjevic, and M. Gyulassy, Nucl. Phys. **A783**, 493 (2007); S. Wicks, W. Horowitz, M. Djordjevic, and M. Gyulassy, *ibid.* **A784**, 426 (2007).
[7] H. Zhang, J. F. Owens, E. Wang, and X.-N. Wang, Phys. Rev. Lett. **98**, 212301 (2007).
[8] L. Aphecetche *et al.*, Nucl. Instrum. Methods A **499**, 511 (2003).
[9] A. Adare *et al.*, arXiv:0801.4020v1 [nucl-ex].
[10] R. Baier, Y. L. Dokshitzer, A. H. Mueller, S. Peigne, and D. Schiff, Nucl. Phys. **B484**, 265 (1997); see also Ref. [3].
[11] C. A. Salgado and U. A. Wiedemann, Phys. Rev. D **68**, 014008 (2003).
[12] I. Vitev, Phys. Lett. **B639**, 38 (2006).
[13] J. D. Bjorken, Phys. Rev. D **27**, 140 (1983).
[14] K. J. Eskola, H. Honkanen, C. A. Salgado, and U. A. Wiedemann, Nucl. Phys. **A747**, 511 (2005).
[15] M. Djordjevic and M. Gyulassy, Nucl. Phys. **A733**, 265 (2004).
[16] C. Loizides (private communcation).
[17] I. Vitev (private communication).
[18] W. Horowitz (private communication).
[19] X.-N. Wang (private communication).
[20] W.-M. Yao *et al.* [Particle Data Group], J. Phys. G **33**, 278 (2006).
[21] R. Baier and D. Schiff, J. High Energy Phys. 09 (2006) 059; R. Baier, A. H. Mueller, and D. Schiff, Phys. Lett. **B649**, 147 (2007).
[22] Attributed to S. S. Wilks in S. L. Meyer, *Data Analysis for Scientists and Engineers*, Library Shelf Mark QA 276 MEYE (Peer Management Consultants, Ltd., reprinted 1992).
[23] F. James, MINUIT Reference Manual, CERN Program Library Long Writeup D506, 1994.
[24] J. Heinrich and L. Lyons, Annu. Rev. Nucl. Part. Sci. **57**, 145 (2007).